J. Astrophys. Astr. (2014) **35,** 157–182

Prospects for Detecting the 326.5 MHz Redshifted 21-cm HI Signal with the Ooty Radio Telescope (ORT)

Sk. Saiyad Ali[1,*] & Somnath Bharadwaj[2]
[1]*Department of Physics, Jadavpur University, Kolkata 700 032, India.*
[2]*Department of Physics and Meteorology & Centre for Theoretical Studies, IIT Kharagpur, Kharagpur 721 302, India.*
[*]*e-mail: saiyad@phys.jdvu.ac.in*

Received 7 October 2013; accepted 13 February 2014

Abstract. Observations of the redshifted 21-cm HI fluctuations promise to be an important probe of the post-reionization era ($z \leq 6$). In this paper we calculate the expected signal and foregrounds for the upgraded Ooty Radio Telescope (ORT) which operates at frequency $\nu_o = 326.5$ MHz which corresponds to redshift $z = 3.35$. Assuming that the visibilities contain only the HI signal and system noise, we show that a 3σ detection of the HI signal (~ 1 mK) is possible at angular scales $11'$ to 3° with $\approx$1000 h of observation. Foreground removal is one of the major challenges for a statistical detection of the redshifted 21 cm HI signal. We assess the contribution of different foregrounds and find that the 326.5 MHz sky is dominated by the extragalactic point sources at the angular scales of our interest. The expected total foregrounds are 10^4–10^5 times higher than the HI signal.

Key words. Cosmology: large scale structure of Universe—intergalactic medium—diffuse radiation.

1. Introduction

The study of the evolution of cosmic structure has been an important subject in cosmology. In the post reionization era ($z < 6$) the 21-cm emission originates from dense pockets of self-shielded hydrogen. These systems which are seen as Damped Lyman-α absorption lines (DLAs) in quasar spectra are known to contain the bulk of the HI (Zafar *et al*. 2013). Different from traditional galaxy redshift surveys, the 21-cm surveys do not need to resolve individual HI sources. The collective emission from the individual clouds appears as a very faint, diffuse background radiation in all low frequency radio observations below 1420 MHz, and the source clustering is imprinted on the fluctuations of this background radiation (Bharadwaj *et al*. 2001). Observations of the redshifted 21-cm radiation from neutral hydrogen (HI) can in principle be carried out over a large redshift range starting from the cosmological dark ages through the Epoch of Reionization (EoR) to the present epoch. This allows

us to study both the evolution history of neutral hydrogen as well as the growth of large scale structures in the Universe (Kumar *et al*. 1995; Bagla *et al*. 1997, 2010; Madau *et al*. 1997; Bharadwaj *et al*. 2001; Bharadwaj & Pandey 2003; Bharadwaj & Ali 2005; Furlanetto *et al*. 2006; Wyithe & Loeb 2008). Redshifted 21-cm observations also hold the potential of probing the expansion history of the Universe (Visbal *et al*. 2009; Bharadwaj *et al*. 2009). It has been proposed that the Baryon Acoustic Oscillation (BAO) in the redshifted 21-cm signal from the post-reionization era ($z \leq 6$) is a very sensitive probe of dark energy (Wyithe *et al*. 2007; Chang *et al*. 2008; Seo *et al*. 2010; Masui *et al*. 2010). A compact interferometer with a wide field-of-view is needed to cover the BAO length-scale. By scanning across frequency, 21 cm observations will probe the HI distribution at different times in cosmic history. It will allow us to construct 21 cm tomography of the IGM. This tomography may carry more useful information than any other survey in cosmology (Madau *et al*. 1997; Loeb & Zaldarriaga 2004; Loeb & Wyithe 2008).

Realizing this great potential, a large number of recent or upcoming radio-interferometric experiments are aimed at measuring the HI 21 cm signal at different redshifts from $z \sim 1$ to 12. The Giant Meterwave Radio Telescope (GMRT[1]; Swarup *et al*. 1991) is functioning at several bands in the frequency range 150–1420 MHz and can potentially detect the 21 cm signal at high as well as low redshifts (Bharadwaj & Ali 2005). Several low-frequency EoR experiments (LOFAR[2], MWA[3], 21CMA, formerly known as PAST[4], PAPER (Parsons *et al*. 2010), LWA[5]) are currently in progress or under construction. They have raised the possibility to detect and characterize the EoR signal. Several other upcoming radio telescopes like CHIME[6] and BAOBAB[7] aim to probe the low redshift Universe ($z \leq 2.5$). It has been recently reported that a cylindrical transit interferometer would be a novel approach which would avoid the curved sky complications of conventional interferometry and be well suited for wide-field observations (Shaw *et al*. 2013). They claim that the data analysis techniques and two point statistics allow new ways of tackling the important problems like map-making and foreground removal. More ambitious designs are being planned for the future low-frequency telescope SKA[8]. This would be well suited for carrying out observations towards detecting the HI signal over a large redshift range $z \sim 0$ to ~ 12.

The removal of continuum foregrounds sources (such as extragalactic point sources, galactic synchrotron, and galactic and extra-galactic free free emission) is a major challenge for detecting the faint HI signal. The foreground sources are expected to be roughly four to five orders of magnitude stronger than the cosmological HI signal (Di Matteo *et al*. 2002; Ali *et al*. 2008; Ghosh *et al*. 2011a). Various proposals for tackling the foreground issue have been discussed in the literature (Harker *et al*. 2009; Bowman *et al*. 2009; Datta *et al*. 2010; Jelic *et al*. 2010;

[1] http://www.gmrt.ncra.tifr.res.in
[2] http://www.lofar.org/
[3] http://web.haystack.mit.edu/ast/arrays/MWA/
[4] http://web.phys.cmu.edu/~past/
[5] http://lwa.nrl.navy.mil/
[6] http://chime.phas.ubc.ca/
[7] http://bao.berkeley.edu/
[8] http://www.skatelescope.org/

Bernardi *et al*. 2011; Ghosh *et al*. 2011b; Liu & Tegmark 2011; Mao 2012; Liu & Tegmark 2012; Cho *et al*. 2012; Switzer *et al*. 2013a, b; Jacobs *et al*. 2013; Pober *et al*. 2013; Dillon *et al*. 2013,). The polarized galactic synchrotron emission is expected to be Faraday-rotated along the path, and it may acquire additional spectral structure through polarization leakage at the telescope. This is a potential complication for detecting the HI signal. The effect of polarized foregrounds on foreground removal has been studied by Moore *et al*. (2013).

A statistical detection of the post-reionization HI signal has already been made (Pen *et al*. 2009) through cross-correlation between the HIPASS and the 6dfGRS. In a recent paper, Masui *et al*. (2010) have measured the cross power spectrum at redshift $z \sim 0.8$ using 21-cm intensity maps acquired at the Green Bank Telescope (GBT) and large-scale structure traced by optically selected galaxies in the WiggleZ Dark Energy Survey. This measurement puts a lower limit on the fluctuation power, of 21 cm emission. For the first time, Switzer *et al*. (2013a, b) have measured the auto-power spectrum of redshifted 21 cm radiation from the HI distribution at redshift $z \sim 0.8$ with GBT. These detections represent important steps towards using redshifted 21 cm surface brightness fluctuations to probe the HI distribution at high z.

Efforts are currently underway (Prasad & Subrahmanya 2011a, b) to upgrade the Ooty Radio Telescope (hereafter ORT) so that it may be operated as a radio-interferometric array. The aim of this paper is to present the expected post-reionization 21 cm signal at a frequency of $\nu_o = 326.5$ MHz ($z = 3.35$), and to discuss the possibility of its detection with the upgraded ORT. For detecting this faint cosmological signal, it is very crucial to understand all foreground components in detail. Here we use a foreground model to predict the foreground contribution to the radio background at 326.5 MHz. The prospect for detecting the redshifted 21 cm signal is considerably higher at this frequency in comparison to the lower frequencies (e.g. 150 MHz, EoR) where the foreground contribution and the system noise are both larger.

The background UV radiation at redshift ($z = 3.35$) is expected to be nearly uniform, and we expect the redshifted 21 cm power spectrum to trace the underlying matter power spectrum with a possible linear bias. The ORT holds the potential of measuring the $z = 3.35$ power spectrum, opening the possibility of probing large-scale structure formation at an hitherto unexplored redshift. We note that it is extremely difficult to accurately measure the redshift for a large number of galaxies at high redshifts (Eisenstein *et al*. 2005), and it will be difficult to probe $z > 3$ using galaxy surveys. Further, the quasar distribution is known to peak between $z = 2$ and 3 (Busca *et al*. 2013), and we do not expect Lyman-α forest surveys to be very effective at $z > 3$. Observations of the redshifted 21-cm signal are possibly one of the few (if not only) techniques by which it will be possible to probe the matter power spectrum at $z > 3$. This has the possibility of probing cosmology and structure formation through a variety of effects including the redshift space distortion (Bharadwaj *et al*. 2001; Bharadwaj & Ali 2004; Barkana & Loeb 2005; Ali *et al*. 2005; Wang & Hu 2006; Masui *et al*. 2010; Mao *et al*. 2012; Majumdar *et al*. 2013) and the Alcock–Paczyski test (Nusser 2005; Barkana 2006). Further, five successive oscillations of the BAO are well in the k range that will be probed by ORT. The BAO is a powerful probe of the expansion history, and a detection will constrain cosmological parameters at $z = 3.35$. The present paper is exploratory in nature, and it presents a preliminary estimate of the expected signal and foregrounds. We

plan to present more quantitative estimates for parameter estimation in subsequent publications.

A brief outline of the paper is as follows: Section 2 introduces the upgraded ORT as a radio interferometer and analyses the visibility signal that will be measured by this instrument. Section 3 discusses how the correlations between the measured visibilities can be used to quantify the angular and frequency domain fluctuations of the background radiation. Section 4 presents model prediction for the HI signal, the signal-to-noise ratio and the contributions from different foregrounds components. This section also discusses the feasibility of detection of the signal. Section 5 contains a summary and conclusions.

In this work we have used the standard LCDM cosmology with parameters: $\Omega_{m0} = 0.30$, $\Omega_b h^2 = 0.024$, $\Omega_{\Lambda 0} = 0.7$, $h = 0.7$, $n_s = 1.0$ and $\sigma_8 = 1.0$.

2. The ORT and the measured visibilities

The Ooty Radio Telescope (ORT) consists of a 530-m long and 30-m wide parabolic cylindrical reflector. The telescope is placed in the North–South direction on a hill with the same slope as the latitude (11°) of the station (Swarup *et al*. 1971; Sarma *et al*. 1975). It thus becomes possible to observe the same part of the sky by rotating the parabolic cylinder along its long axis. The telescope operates at a nominal frequency of $\nu_o = 326.5$ MHz with $\lambda_o = 0.919$ m. The entire telescope feed consists of 1056 half-wavelength ($0.5\,\lambda_o \approx 0.5$ m) dipoles which are placed nearly end-to-end along the focal line of the cylinder. The separation between the centres of two successive dipoles is $0.515\,\lambda_o$ which is slightly larger than the length of each dipole. The entire feed is placed off-axis to avoid maximally the obstruction of the incoming radiation.

Work is currently underway to upgrade the ORT whereby the linear dipole array may be operated as a radio-interferometer. Here the signal from groups of dipoles is combined to form an antenna element. The RF signal from each antenna element is directly digitized and transported to a central location where the signals from different pairs of antenna elements are correlated to produce the visibilities $\mathcal{V}(\mathbf{U}, \nu)$ which are recorded. Here $\mathbf{U} = \vec{d}/\lambda$ refers to a baseline which is the antenna separation (Fig. 1), $\vec{d}$ in units of the observing wavelength λ. The upgrade is being carried out in two different stages with two nearly independent systems, namely Phase I and Phase II, being expected at the end of the upgrade (Prasad & Subrahmanya 2011a, b). We briefly discuss these two phases below, and the relevant parameters are presented in Table 1 (Subrahmanya, private communication).

Phase I: Here 24 successive dipoles are combined to form a single antenna element. This gives 40 antennas each of which is 11.5 m along the length of the cylinder and 30 m wide. The smallest baseline corresponds to an antenna separation of 11.5 m and the longest baseline corresponds to 448.5 m. The system has a frequency bandwidth of 18 MHz.

Phase II: Here 4 successive dipoles are combined to form a single antenna element. This gives 264 antennas each of which is 1.9 m along the length of the cylinder and 30 m wide. The smallest baseline also corresponds to an antenna separation of

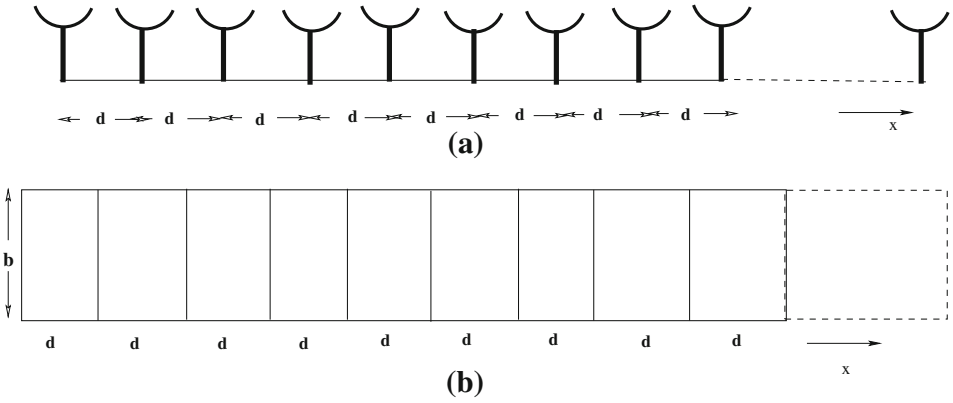

Figure 1. This shows the antenna layout corresponding to the ORT when it is used as a radio-interferometer. We have a linear array of antenna elements with spacing d arranged along the x axis which is aligned to the axis of the cylindrical reflector. The figure also shows the $b \times d$ rectangular aperture of the individual antenna elements. Here b corresponds to the width of the parabolic cylindrical reflector.

1.9 m and the longest baseline corresponds to 505.0 m. The system has a frequency bandwidth of 30 MHz.

We note that CHIME, an upcoming new telescope designed to detect the BAO, is partly similar to the ORT in construction. The CHIME consists of five parabolic cylindrical reflectors, each of dimensions 100 m × 20 m and each containing 256 antennas. The total telescope is 100 m × 100 m in dimension. Unlike the ORT, this will be a drift scan telescope with no moving parts, and it will cover the frequency range 800 to 400 MHz which corresponds to the redshift range ∼0.8 to 2.5.

Figure 1 provides a schematic representation of the ORT when it is used as a radio-interferometer. The parabolic cylinder may be thought of as a linear array of N_A radio antennas, each antenna located at a separation d along the length of the cylinder. Viewed from the direction in which the telescope is pointing, each antenna has a rectangular aperture of dimensions $b \times d$ where $b = 30$ m is the width of the parabola, and $d = 11.5$ and 1.9 m for Phases I and II respectively. For convenience,

Table 1. System parameters for phases I and II of the upgraded ORT.

Parameter	Phase I	Phase II
No. of antennas (N_A)	40	264
Aperture dimensions ($b \times d$)	30 m × 11.5 m	30 m × 1.92 m
Field-of-View (FoV)	1.75° × 4.6°	1.75° × 27.4°
Smallest baseline ($d_{\rm min}$)	11.5 m	1.9 m
Largest baseline ($d_{\rm max}$)	448.5 m	505.0 m
Angular resolution	$7'$	$6.3'$
Total bandwidth (**B**)	18 MHz	30 MHz
Single visibility rms. noise (σ) assuming $T_{\rm sys} = 150$ K, $\eta = 0.6$, $\Delta\nu_{\rm c} = 0.1$ MHz, $\Delta t = 16$ s	1.12 Jy	6.69 Jy

we have assumed the telescope aperture to lie in the $x-y$ plane with the x axis along the length of the cylinder. We then have the baselines

$$\mathbf{U}_1 = \left(\frac{d}{\lambda}\right)\hat{i}; \quad \mathbf{U}_2 = 2\mathbf{U}_1; \quad \mathbf{U}_3 = 3\mathbf{U}_1; \ldots; \quad \mathbf{U}_{N_A-1} = (N_A-1)\mathbf{U}_1 \quad (1)$$

for which the complex visibilities $\mathcal{V}(\mathbf{U}, \nu)$ are recorded. It should be noted that there is considerable redundancy in this radio-interferometric array i.e. there are many different antenna pairs which correspond to the same baseline. Any baseline $\mathbf{U}_n$ occurs $M_n = (N_A - n)$ times in the array. In reality $\mathbf{U}_1, \mathbf{U}_2, \ldots$ change as ν varies across the observing bandwidth. This is an extremely important factor that needs to be considered in the actual data analysis. However this is not very significant for the signal and foreground estimates presented here, and we ignore this for the purpose of the present analysis, and hold $\mathbf{U}$ fixed at the value corresponding to λ_o.

The visibility $\mathcal{V}(\mathbf{U}, \nu)$ recorded at any baseline $\mathbf{U}$ is the Fourier transform of the product of $I(\vec{\theta}, \nu)$ which is the specific intensity distribution on the sky and $A(\vec{\theta}, \nu)$ which is the primary beam pattern or the normalized power pattern of the individual antenna. We have

$$\mathcal{V}(\mathbf{U}, \nu) = \int d^2\vec{\theta} A(\vec{\theta}, \nu) I(\vec{\theta}, \nu) \mathrm{e}^{-i2\pi \mathbf{U}\cdot\vec{\theta}}. \quad (2)$$

where $\vec{\theta}$ is a two dimensional vector in the plane of the sky with origin at the centre of the field-of-view, and the beam pattern $A(\vec{\theta}, \nu)$ quantifies how the individual antenna responds to signals from different directions in the sky. We have assumed that the field-of-view of the individual antennas is sufficiently small so that we may ignore the curvature of the sky and treat the region of sky under observation as being flat. While such an assumption is quite justified for Phase I, the field-of-view is quite large for Phase II and the flat sky assumption is not strictly valid in this situation. We, however, expect our predictions based on the flat sky assumption to provide a reasonable preliminary estimate of the signal expected for both Phases I and II.

We now briefly discuss the normalized power pattern $A(\vec{\theta}, \nu)$ of the individual antennas in our radio-interferometer. This can be calculated by considering the antenna as an emitter instead of receiver. We first calculate $E(\vec{\theta}, \nu)$, the normalized far-field radiation electric pattern that will be produced by the antenna, where $A(\vec{\theta}, \nu) = \mid E(\vec{\theta}, \nu) \mid^2$. The function $E(\vec{\theta}, \nu)$ is the Fourier transform of the electric field pattern $\tilde{E}(\mathbf{U}, \nu)$ at the telescope's aperture (Fig. 1). The ORT responds only to a single polarization determined by the dipole feeds which are aligned parallel to the telescope cylinder's axis. It is therefore justified to ignore the vector nature of the electric field $\tilde{E}(\mathbf{U}, \nu)$ and focus on a single polarization. The exact form of $\tilde{E}(\mathbf{U}, \nu)$ depends on how the dipole illuminates the antenna aperture. Modeling this is quite complicated and we do not attempt it here. For the purpose of the present analysis, we make the simplifying assumption that the electric field $\tilde{E}(\mathbf{U}, \nu)$ is uniform everywhere on the $b \times d$ rectangular aperture of the antenna element (Fig. 1). We then have the primary beam pattern

$$A(\vec{\theta}, \nu) = \mathrm{sinc}^2\left(\frac{\pi d\theta_x}{\lambda}\right) \mathrm{sinc}^2\left(\frac{\pi b\theta_y}{\lambda}\right). \quad (3)$$

The actual beam pattern is expected to be somewhat broader than that predicted by eq. (3) if the dipole's illumination pattern is taken into account. We use the aperture efficiency η that appears in the subsequent calculations to account for this to some extent.

The primary beam pattern decides the field-of-view of the radio-interferometer. We see that in this case (eq. (3)) we have an asymmetric field-of-view. The primary beam has a Full Width at Half Maximum (FWHM) of 1.55° corresponding to $b = 30$ m in the East–West direction, and 4.05° and 24.32° in the North–South direction for Phases I and II respectively. The anisotropy in the field-of-view is particularly pronounced in Phase II where the N–S extent is more than 10 times the extent in the E–W direction.

It is useful to decompose the specific intensity as

$$I(\vec{\theta}, \nu) = \bar{I}(\nu) + \delta I(\vec{\theta}, \nu), \tag{4}$$

where the first term is an uniform background brightness and the second term is the angular fluctuation in the specific intensity. We use this and express eq. (2) in terms of a convolution as

$$\mathcal{V}(\mathbf{U}, \nu) = \tilde{A}(\mathbf{U}, \nu)\, \bar{I}(\nu) + \tilde{A}(\mathbf{U}, \nu) \otimes \Delta\tilde{I}(\mathbf{U}, \nu), \tag{5}$$

where $\Delta\tilde{I}(\mathbf{U}, \nu)$ and $\tilde{A}(\mathbf{U}, \nu)$ are the Fourier transforms of $\delta I(\vec{\theta}, \nu)$ and $A(\vec{\theta}, \nu)$ respectively. We refer to $\tilde{A}(\mathbf{U}, \nu)$ as the aperture power pattern.

The aperture power pattern $\tilde{A}(\mathbf{U}, \nu)$ is the auto-convolution of the electric field at the telescope aperture i.e., $\tilde{A}(\mathbf{U}, \nu) = \tilde{E}(\mathbf{U}, \nu) \otimes \tilde{E}(\mathbf{U}, \nu)$. The telescope's aperture being finite, we have the interesting property that $\tilde{A}(\mathbf{U}, \nu)$ has compact support in $\mathbf{U}$ irrespective of the details of the shape of the telescope's aperture. For the uniform rectangular aperture assumed earlier, we have

$$\tilde{A}(\mathbf{U}, \nu) = \frac{\lambda^2}{bd} \Lambda\left(\frac{u\,\lambda}{d}\right) \Lambda\left(\frac{v\,\lambda}{b}\right), \tag{6}$$

where $\mathbf{U} = (u, v)$, and $\Lambda(x)$ is the triangular function defined as

$$\Lambda(x) = 1 - |x| \quad \text{for } |x| < 1, \qquad \text{and} \qquad \Lambda(x) = 0 \quad \text{for } |x| \geq 1. \tag{7}$$

We see that $\tilde{A}(\mathbf{U}, \nu)$ has non-zero values only within $|\, u \,| < d/\lambda$, $|\, v \,| < b/\lambda$ and vanished beyond. Figure 2 shows the u dependence of $\tilde{A}(\mathbf{U}, \nu)$ for $v = 0$. The actual behaviour of $\tilde{A}(\mathbf{U}, \nu)$ will be different, and we expect the u, v dependence to fall faster than the triangular function when the dipole's illumination pattern is taken into account. However the fact that $\tilde{A}(\mathbf{U}, \nu)$ has compact support, and that $\tilde{A}(\mathbf{U}, \nu) = 0$ for $|\, u \,| \geq d/\lambda$, $|\, v \,| \geq b/\lambda$ will continue to hold.

We see that the first term $\tilde{A}(\mathbf{U}, \nu)\, \bar{I}(\nu)$ in eq. (5) dies away before the smallest baseline $\mathbf{U}_1$ (Fig. 2), and hence it is not necessary to consider the contribution from $\bar{I}_\nu$. We then have

$$\mathcal{V}(\mathbf{U}_n, \nu) = \int d^2U' \tilde{A}(\mathbf{U}_n - \mathbf{U}', \nu) \Delta\tilde{I}(\mathbf{U}', \nu). \tag{8}$$

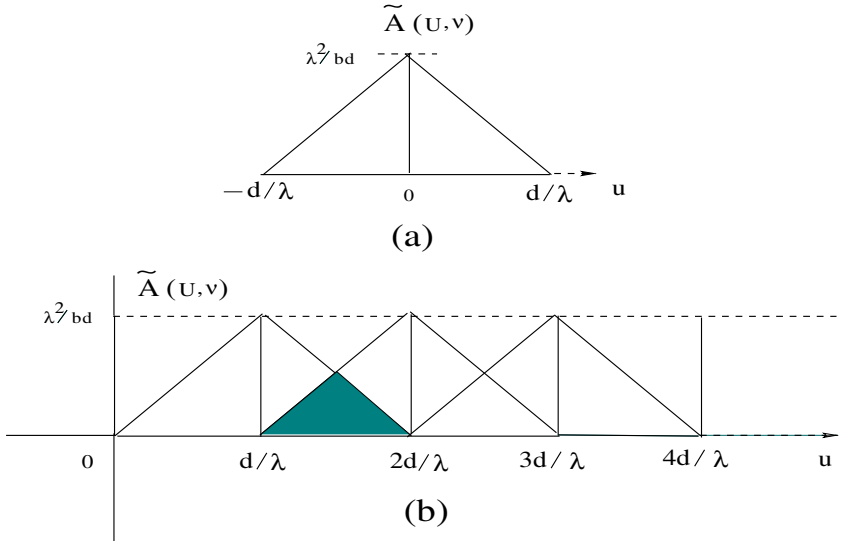

Figure 2. The upper panel shows a schematic view of the aperture power pattern $\tilde{A}(\mathbf{U}, \nu)$ as a function of u for $v = 0$. The lower panel shows the u range and the respective weights corresponding to each Fourier mode that contributes to the visibility at any baseline $\mathbf{U}_n$. The shaded region shows the overlap between the Fourier modes that contribute to the visibilities at two adjacent baselines.

where each visibility $\mathcal{V}(\mathbf{U}_n, \nu)$ is a weighted linear superposition of different Fourier modes $\Delta\tilde{I}(\mathbf{U}, \nu)$. The contribution peaks at $\mathbf{U} = \mathbf{U}_n$, and it is restricted to a rectangle of size $(b/\lambda) \times (d/\lambda)$ centered at $\mathbf{U}_n$. The modes outside this region do not contribute to $\mathcal{V}(\mathbf{U}_n, \nu)$. This is shown schematically in Fig. 2. We also note that there is an overlap between the Fourier modes that contribute to two neighbouring visibilities $\mathcal{V}(\mathbf{U}_n, \nu)$ and $\mathcal{V}(\mathbf{U}_{n+1}, \nu)$. This implies that to some extent the same information is present in the visibilities measured at two neighbouring baselines. This overlap, however, is restricted to the nearest neighbours, and does not extend beyond.

In addition to the sky signal discussed till now, each visibility also has a noise contribution i.e.,

$$\mathcal{V}(\mathbf{U}_n, \nu) = \mathcal{V}^{\mathrm{sky}}(\mathbf{U}_n, \nu) + \mathcal{N}(\mathbf{U}_n, \nu), \tag{9}$$

where the noise contribution $\mathcal{N}(\mathbf{U}_n, \nu)$ in each visibility is an independent complex Gaussian random variable with zero mean. The real part (or equivalent to the imaginary part) of $\mathcal{N}(\mathbf{U}_n, \nu)$ has a rms fluctuation (Thompson *et al.* 1986)

$$\sigma = \frac{\sqrt{2}k_{\mathrm{B}}T_{\mathrm{sys}}}{\eta A\sqrt{\Delta\nu_{\mathrm{c}}\Delta t}}, \tag{10}$$

where T_{sys} is the total system temperature, k_{B} is the Boltzmann constant, $A = b \times d$ is the physical collecting area of each antenna, η is the aperture efficiency, $\Delta\nu_{\mathrm{c}}$ is the channel width and Δt is the correlator integration time. We expect T_{sys} to have a value around 150 K, and we use this value for the estimates presented here. Considering observations with $\Delta\nu_{\mathrm{c}} = 0.1$ MHz and $\Delta t = 16$ s we have $\sigma = 1.12$ Jy and 6.69 Jy for Phases I and II respectively.

We now highlight two interesting features which are unique to the ORT radio-interferometer. First, in a typical radio-interferometer the baseline $\mathbf{U}$ corresponding to a pair of antennas changes with the rotation of the Earth. As a consequence, the individual baselines sweep out different tracks in the $u - v$ plane during the course of a long observation. However, for the ORT, the North–South axis of the cylindrical reflector is parallel to the Earth's rotation axis. The baselines (eq. (1)) too are all parallel to the Earth's rotation axis and they do not change with the rotation of the Earth. Second, the interferometer has a high degree of redundancy in that there are $N_A - n$ distinct antenna pairs which correspond to any particular baseline $\mathbf{U}_n$. Considering a particular baseline $\mathbf{U}_m$, the visibility $\mathcal{V}'_{ab}$ measured by any antenna pair a, b is the actual visibility $\mathcal{V}(\mathbf{U}_m)$ amplified by the unknown individual antenna gains g_a and g_b i.e. $\mathcal{V}'_{ab} = g_a\, g_b^* \mathcal{V}(\mathbf{U})$. The fact that there are many different antenna pairs for which the measured visibility has the same signal $\mathcal{V}(\mathbf{U}_m)$ can be put to good use in determining the unknown antenna gains g_a and g_b (Ram Marthi & Chengalur 2013).

3. Visibility correlations

We assume that the observed sky signal $\delta I(\vec{\theta},\ \nu)$ is a particular realization of a statistically homogeneous and isotropic random process. In other words, the process that generates $\delta I(\vec{\theta},\ \nu)$ has no preferred origin or direction on the sky. Further, it also has no preferred origin in frequency. We use the multi-frequency angular power spectrum $C_\ell(\Delta\nu)$ to quantify the statistical properties of $\delta I(\vec{\theta},\ \nu)$ (Datta *et al.* 2007). The calculations are considerably simplified in the flat-sky approximation where it is convenient to use Fourier modes instead of the spherical harmonics $Y_\ell^m(\theta, \phi)$. The two-dimensional power spectrum $P(U, \Delta\nu)$ is defined through

$$\langle \Delta\tilde{I}(\mathbf{U},\ \nu)\Delta\tilde{I}^*(\mathbf{U}',\ \nu + \Delta\nu)\rangle = P(U, \Delta\nu)\delta_{\mathrm{D}}^2(\mathbf{U} - \mathbf{U}'), \tag{11}$$

where $\delta_{\mathrm{D}}^2\left(\mathbf{U} - \mathbf{U}'\right)$ is the two-dimensional Dirac-delta function. The angular brackets $\langle\cdots\rangle$ above denote the ensemble average with respect to different realizations of $\delta I(\vec{\theta},\ \nu)$.

The multi-frequency angular power spectrum $C_\ell(\Delta\nu)$ refers to $\delta T(\vec{\theta},\ \nu)$ which is the brightness temperature corresponding to $\delta I(\vec{\theta},\ \nu)$. We have

$$C_\ell(\Delta\nu) = \left(\frac{\partial B}{\partial T}\right)^{-2} P(\ell/2\pi, \Delta\nu)\,, \tag{12}$$

where the angular multipole ℓ corresponds to the 2D dimensional wave vector $2\pi\mathbf{U}$ with $\ell = 2\pi|\mathbf{U}|$, B is the Planck function and $(\partial B/\partial T) = 2k_B/\lambda^2$ in the Raleigh–Jeans limit which is valid at the frequencies of our interest. Strictly speaking, we should evaluate $(\partial B/\partial T)$ at two different frequencies ν and $\nu + \Delta\nu$. This introduces a slow variation of order $\sim \Delta\nu/\nu$ which is small in most of our analysis. For the estimates of this paper, here and in subsequent analysis, we ignore several such terms which introduce slow variations of the order of $\sim\Delta\nu/\nu \ll 1$.

The multi-frequency angular power spectrum $C_\ell(\Delta\nu)$ defined above jointly characterizes the angular (ℓ) and frequency ($\Delta\nu$) dependence of the statistical properties

of the sky signal. The observed visibilities $\mathcal{V}(\mathbf{U}_n, \nu)$ are related to $C_\ell(\Delta\nu)$ through the two visibility correlation which, using eqs (8), (11) and (12) can be written as

$$\langle \mathcal{V}(\mathbf{U}_n, \nu)\, \mathcal{V}^*(\mathbf{U}_m, \nu + \Delta\nu)\rangle = \left(\frac{\partial B}{\partial T}\right)^2 \int d^2U'\, \tilde{A}(\mathbf{U}_n - \mathbf{U}', \nu) \times \tilde{A}^*(\mathbf{U}_m - \mathbf{U}', \nu + \Delta\nu)\, C_{2\pi U'}(\Delta\nu)\,. \quad (13)$$

The functions $\tilde{A}(\mathbf{U}_n - \mathbf{U}', \nu)$ and $\tilde{A}^*(\mathbf{U}_m - \mathbf{U}', \nu + \Delta\nu)$ have an overlap only when $\mid n - m \mid \leq 1$ (Fig. 1). This implies that two visibilities are correlated only if they correspond to the same baseline or the nearest neighbours. The correlation is strongest when $n = m$, and we restrict our analysis here to this situation where the two baselines are the same. Further, in subsequent discussions we also ignore the slow $\Delta\nu$ dependence of $\tilde{A}^*(\mathbf{U}_m - \mathbf{U}', \nu + \Delta\nu)$. The two visibility correlation can then be expressed as

$$V_2(\mathbf{U}_n, \Delta\nu) \equiv \langle \mathcal{V}(\mathbf{U}_n, \nu)\mathcal{V}^*(\mathbf{U}_n, \nu + \Delta\nu)\rangle \quad (14)$$

and we have

$$V_2(\mathbf{U}_n, \Delta\nu) = \left(\frac{\partial B}{\partial T}\right)^2 \int d^2\mathbf{U}'\, |\tilde{A}\left(\mathbf{U}_n - \mathbf{U}'\right)|^2\, C_{2\pi\, U'}(\Delta\nu), \quad (15)$$

where we do not explicitly show ν as an argument in any of the terms, and it is implicit that this has the value $\nu_o = 326.5\,\mathrm{MHz}$.

At large baselines it is possible to approximate the convolution in eq. (15) as

$$V_2(\mathbf{U}_n, \Delta\nu) = \left(\frac{\partial B}{\partial T}\right)^2 \left[\int d^2\mathbf{U}'\, |\tilde{A}\left(\mathbf{U}_n - \mathbf{U}'\right)|^2\right] C_\ell(\Delta\nu) \quad (16)$$

with $\ell = 2\pi U_n$. This gives a very simple relation

$$C_\ell(\Delta\nu) = 0.26 \left(\frac{\mathrm{mK}}{\mathrm{Jy}}\right)^2 \left(\frac{b\; d}{\mathrm{m}^2}\right) V_2(\mathbf{U}_n, \Delta\nu) \quad (17)$$

between $V_2(\mathbf{U}_n, \Delta\nu)$ which can be determined directly from the measured visibilities and $C_\ell(\Delta\nu)$ which quantifies the statistical properties of the brightness temperature distribution on the sky. We expect eq. (17) to be a good approximation only at large baselines where the value of $C_{2\pi\mathbf{U}}(\Delta\nu)$ does not change much within the width of the function $|\tilde{A}\,(\mathbf{U}_n - \mathbf{U})\,|^2$. However, our investigations later in this paper show that eq. (17) provides a reasonable good approximation to the full convolution (eq. (15)) for nearly the entire U range covered by ORT.

4. Predictions

The contribution to the measured visibilities $\mathcal{V}(\mathbf{U}, \nu)$ from the sky signal (eq. (9)) is a combination of two different components

$$\mathcal{V}^{sky}(\mathbf{U}_n, \nu) = \mathcal{S}(\mathbf{U}_n, \nu) + \mathcal{F}(\mathbf{U}_n, \nu)\,, \quad (18)$$

where $\mathcal{S}(\mathbf{U}_n, \nu)$ is the HI signal which is the object of our study here, and $\mathcal{F}(\mathbf{U}_n, \nu)$ is the contribution from other astrophysical sources referred to as the foregrounds. We treat both of these, as well as the system noise $\mathcal{N}(\mathbf{U}_n, \nu)$ as uncorrelated random variables with zero mean. We then have

$$V_2(\mathbf{U}_n, \Delta\nu) = S_2(\mathbf{U}_n, \Delta\nu) + F_2(\mathbf{U}_n, \Delta\nu) + N_2(\mathbf{U}_n, \Delta\nu), \tag{19}$$

where S_2, F_2 and N_2 respectively refer to signal, foreground and noise contributions to the visibility correlation. We individually discuss the predictions for each of these components.

4.1 *The HI signal*

The contribution $S_2(\mathbf{U}_n, \Delta\nu)$ to the visibility correlation $V_2(\mathbf{U}, \Delta\nu)$ from the HI signal directly probes the three-dimensional (3D) power spectrum $P_{\rm HI}(\mathbf{k}, z)$ of the HI distribution in redshift space (Bharadwaj & Sethi 2001; Bharadwaj & Ali 2005). It is convenient to use

$$C_\ell(\Delta\nu) = \frac{1}{\pi r_\nu^2} \int_0^\infty {\rm d}k_\parallel \, \cos(k_\parallel \, r'_\nu \, \Delta\nu) \, P_{\rm HI}(\mathbf{k}) \tag{20}$$

to calculate the multi-frequency angular power spectrum for the HI signal (Datta *et al*. 2007), and use this in eq. (15) to calculate $S_2(\mathbf{U}_n, \Delta\nu)$. Here r_ν is the comoving distance corresponding to $z = (1420\,{\rm MHz}/\nu) - 1$, $r'_\nu = \frac{dr_\nu}{d\nu}$ and the 3D wave vector $\mathbf{k}$ has components $k_\parallel$ and $k_\perp = \ell/r$ which are respectively parallel and perpendicular to the line-of-sight, and $\mu = k_\parallel/k$ is the cosine of the angle between $\mathbf{k}$ and the line-of-sight.

We model $P_{\rm HI}(k, \mu) \equiv P_{\rm HI}(\mathbf{k})$ assuming that HI traces the total matter distribution with a linear, scale-independent bias parameter b. We then have

$$P_{\rm HI}(k, \mu) = b^2 \, \bar{x}_{\rm HI}^2 \, \bar{T}^2 \, [1 + \beta \, \mu^2]^2 \, P(k), \tag{21}$$

where $P(k)$ is the matter power spectrum at the redshift z, $\bar{x}_{\rm HI}$ is the mean hydrogen neutral fraction and

$$\bar{T}(z) = 4.0\,{\rm mK}\,(1+z)^2 \left(\frac{\Omega_b h^2}{0.024}\right) \left(\frac{0.7}{h}\right) \left(\frac{H_0}{H(z)}\right). \tag{22}$$

We have used the value $\bar{x}_{\rm HI} = 2.45 \times 10^{-2}$ which corresponds to $\Omega_{\rm gas} = 10^{-3}$ (Noterdaeme *et al*. 2012; Zafar *et al*. 2013). The term $[1 + \beta\mu^2]^2$ arises due to the HI peculiar velocities (Bharadwaj *et al*. 2001; Bharadwaj & Ali 2004) and β is the linear distortion parameter. The semi-emperical estimate of the large-scale bias (b) of HI at redshift $z \sim 3$ is 1.7 (Marín *et al*. 2010). N-body simulations (Bagla *et al*. 2010; Guha Sarkar *et al*. 2012) indicate that it is reasonably well justified to assume a constant HI bias $b = 2$ at wave numbers $k \leq 1\,{\rm Mpc}^{-1}$, and we have used this value for our entire analysis. The later result is consistent with Marín *et al*. (2010).

Figure 3 shows $k^3 P_{\rm HI}(k)/2\pi^2$ which quantifies the magnitude of the expected HI signal. In this figure we have fixed $\mu = 0$ (eq. (21)) which implies that the wave vector $\mathbf{k}$ is perpendicular to the line-of-sight. The figure also shows the range of

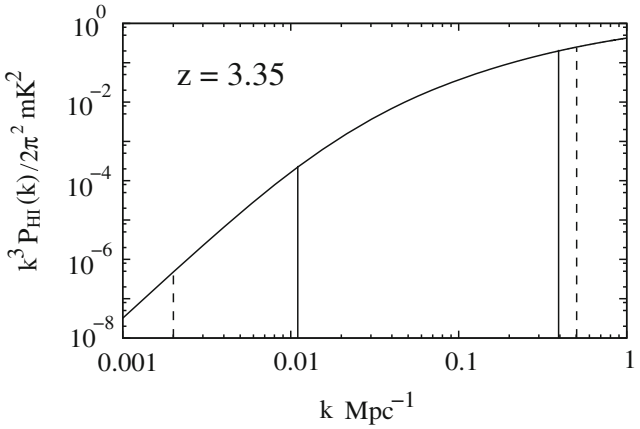

Figure 3. The solid curve shows the HI signal $k^3\, P_{\rm HI}(k)/2\,\pi^2$ where $P_{\rm HI}(k) \equiv P_{\rm HI}(k, \mu = 0)$ is the HI power spectrum (eq. (21)) at $z = 3.35$ which corresponds to $\nu_o = 326.5$ MHz. The vertical lines demarcate the $\mathbf{k}_\perp = \frac{2\pi \mathbf{U}}{r_\nu}$ range that will be probed through the HI signal at ORT. The solid and dashed vertical lines refer to Phases I and II respectively.

comoving wave numbers k where the HI power spectrum $P_{\rm HI}(k)$ will be probed by the ORT. We see that the upper limit $\sim 0.5\,{\rm Mpc}^{-1}$ is comparable in both Phases I and II. The lower limit $\sim 0.002\,{\rm Mpc}^{-1}$, however, is considerably smaller for Phase II in comparison to Phase I which is only sensitive to modes $k > 0.01\,{\rm Mpc}^{-1}$. We note that Phases I and II are both sensitive to the BAO feature which has the first peak at $k = 0.045\,{\rm Mpc}^{-1}$, and which has successive oscillations whose amplitude decays within $k = 0.3\,{\rm Mpc}^{-1}$ which is well within the k range that will be probed by ORT. It is planned to investigate the possibility of detecting the BAO feature and constraining cosmological parameters in a separate, future study.

Our subsequent discussion is in terms of the angular multipole ℓ, baseline U and frequency separation $\Delta\nu$. Here we briefly discuss how these quantities are related to the comoving wave numbers $k_\perp$, $k_\parallel$ and $\Delta r_\parallel$ which is the comoving distance interval along the line-of-sight. We have

$$k_\perp = \frac{2\pi U}{r_\nu} = \frac{\ell}{r_\nu} \tag{23}$$

which relates ℓ and U to $k_\perp$ which is the wave number perpendicular to the line-of-sight. Further, we have

$$\Delta r_\parallel = r'_\nu\, \Delta\nu = \frac{c\, \Delta\nu}{\nu_e a^2 H(a)} \tag{24}$$

which relates $\Delta\nu$ to $\Delta r_\parallel$. The comoving wave number $k_\parallel$, which is parallel to the line-of-sight, is the Fourier conjugate of $\Delta r_\parallel$. We have $r_\nu = 6.67\,{\rm Gpc}$ and $r'_\nu = 11.33\,{\rm Mpc}\, MHz^{-1}$ at $\nu_0 = 326.5$ MHz for which the conversion factors are summarized in Table 2.

We have used the HI power spectrum $P_{\rm HI}(\mathbf{k})$ to calculate the multi-frequency angular power spectrum $C_\ell(\Delta\nu)$ (eq. (20)). The HI signal is maximum when $\Delta\nu = 0$, and Fig. 4 shows $C_\ell(0)$ as a function of ℓ. The respective ℓ range that will be probed by Phases I and II is also indicated in the figure. The value of $C_\ell(0)$ is around

Table 2. Conversion factors for $\nu_o = 326.5$ MHz.

$k_\perp$	U	ℓ	$\Delta\nu$	$\Delta r_\parallel$
$0.01\,\mathrm{Mpc}^{-1}$	11	67	0.1 MHz	1.13 Mpc

$4 \times 10^{-6}\,\mathrm{mK}^2$ at the smallest ℓ values ($\ell \lesssim 150$) where $C_\ell(0)$ is nearly constant independent of ℓ. Beyond this, the value of $C_\ell(0)$ decreases gradually, and we have around $4 \times 10^{-7}\,\mathrm{mK}^2$ at $\ell \approx 3,300$ which is near the largest ℓ mode that will be probed.

We now discuss the visibility correlation HI signal $S_2(\mathbf{U}, \Delta\nu)$ predicted for the ORT (eq. (15)). The signal is maximum for $\Delta\nu = 0$, and we first study $S_2(\mathbf{U}, 0)$ as a function of U as shown in Fig. 5. For Phase II we see that $S_2(\mathbf{U}, 0)$ has a value $3 \times 10^{-7}\,\mathrm{Jy}^2$ at the smallest baseline, and it is nearly constant at small baselines $U \lesssim 30$ beyond which it slowly falls to a value of around $2 \times 10^{-8}\,\mathrm{Jy}^2$ at $U \approx 550$. The U range is considerably smaller for Phase I where $S_2(\mathbf{U}, 0)$ has a value $\sim 4 \times 10^{-8}\,\mathrm{Jy}^2$ at the smallest baseline ($U \approx 10$) and falls to $\sim 5 \times 10^{-9}\,\mathrm{Jy}^2$ at $U \approx 420$.

The visibility correlation $V_2(U, \Delta\nu)$ depends on the size of the antenna aperture through the factor $|\tilde{A}(\mathbf{U}, \nu)|^2$ which appears in eq. (15). The amplitude (eq. (6)) scales as $|\tilde{A}(\mathbf{U}, \nu)|^2 \propto (bd)^{-2}$ whereas the region in $\mathbf{U}$ space where this function has support scales as $\propto (bd)$. As a consequence it follows that we expect the scaling $V_2(\mathbf{U}, \Delta\nu) \propto (bd)^{-1}$, and we expect $(bd) \times V_2(\mathbf{U}, \Delta\nu)$ to be independent of the size of the antenna aperture. This is also apparent from eq. (17) which relates $(bd) \times V_2(\mathbf{U}, \Delta\nu)$ to $C_\ell(\Delta\nu)$, and which is expected to hold if the baseline U is sufficiently large. Figure 4 shows $(bd) \times S_2(\mathbf{U}, 0)$ as a function of U. We find that the

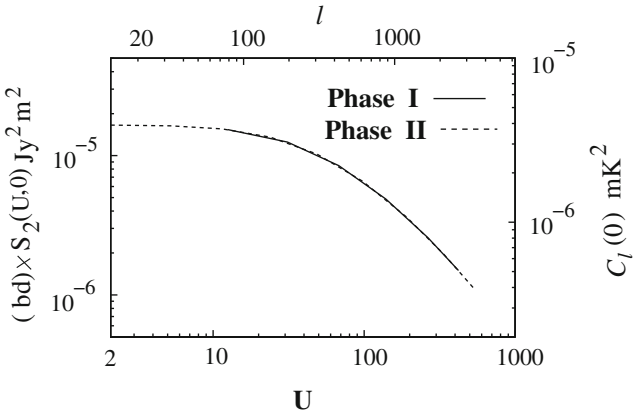

Figure 4. This shows $C_\ell(0)$ and also $(bd) \times S_2(\mathbf{U}, 0)$ which is expected to be independent of the size of the antenna aperture. We find that the values of $(bd) \times S_2(\mathbf{U}, 0)$ predicted for Phase I are nearly identical to those predicted for Phase II, and it is not possible to distinguish between the two curves in the figure. However, as shown in the figure, the U range covered by Phase I is smaller.

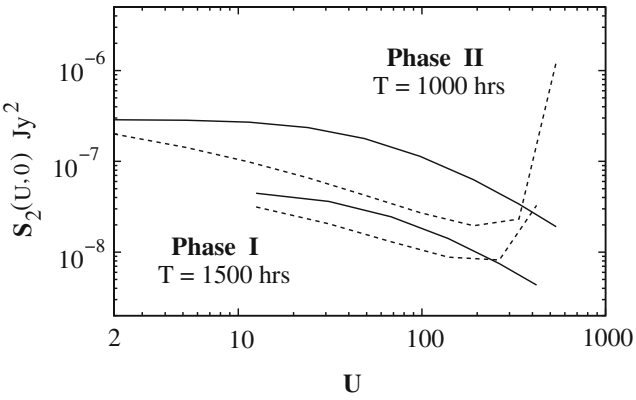

Figure 5. The solid curves show the expected HI signal $S_2(\mathbf{U}, \Delta\nu)$ for $\Delta\nu = 0$ while the dashed curves show the $1-\sigma$ errors for the observation time indicated in the figure. The lower and upper sets of curves correspond to Phases I and II respectively.

predictions for Phase I are nearly identical to those for Phase II, and it is not possible to distinguish between the two curves in the figure. Based on this we conclude that it is adequate to use eq. (17) to relate the visibility correlation $S_2(U, 0)$ to the multi-frequency angular power spectrum $C_\ell(0)$ of the HI signal for the entire baseline range at ORT. Further, we also expect this to hold for other values of $\Delta\nu$, as well as for the foreground $F_2(U, \Delta\nu)$.

We now quantify the $\Delta\nu$ dependence of the HI signal $S_2(\mathbf{U}, \Delta\nu)$. We use the frequency decorrelation function $\kappa_\mathbf{U}(\Delta\nu)$ (Datta *et al*. 2007) which is defined as

$$\kappa_\mathbf{U}(\Delta\nu) = \frac{S_2(U, \Delta\nu)}{S_2(U, 0)} \,. \tag{25}$$

This function quantifies how quickly the HI signal decorrelates as we increase the frequency separation $\Delta\nu$. The signal is perfectly correlated at $\Delta\nu = 0$ where we have $\kappa_U(0) = 1$, and the correlation falls to $(\kappa_U(\Delta\nu) < 1)$ as $\Delta\nu$ is increased. Figure 6 shows the variation of $\kappa_U(\Delta\nu)$ as a function of $\Delta\nu$ for different values of U. Here

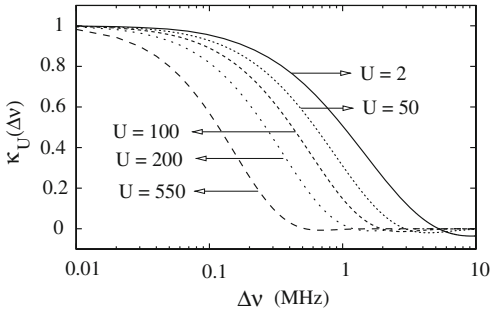

Figure 6. This shows the predicted frequency decorrelation function $\kappa_\mathbf{U}(\Delta\nu)$ as a function of $\Delta\nu$ at five different $\mathbf{U}$ values. The signal decorrelates more sharply for higher values of $\mathbf{U}$.

we have assumed the statistics of the HI signal is stationary across frequency, and thereby only depends on $\Delta\nu$. The predictions are the same for Phases I and II, and we do not show separate curves for the two phases.

We see that at the smallest baseline $U \approx 2$ the value of $\kappa_U(\Delta\nu)$ decreases slowly as $\Delta\nu$ is increased. We have $\kappa_U = 0.5$ at $\Delta\nu \approx 1$ MHz, beyond which the value of κ falls further. The value of κ_U crosses zero at around $\Delta\nu \approx 4$ MHz, and κ_U becomes negative beyond this. The decorrelation function $\kappa_U(\Delta\nu)$ shows a similar $\Delta\nu$ dependence at larger baselines, with the difference that we have a steeper $\Delta\nu$ dependence at larger baselines. For $U = 200$, we see that $\kappa_U = 0.5$ at $\Delta\nu \approx 0.2$ MHz and κ_U crosses zero well before $\Delta\nu = 1$ MHz. We also see that the value of κ_U oscillates round zero for large values of $\Delta\nu$. We have defined $\Delta_{0.5}$ and $\Delta_{0.1}$ as the values of the frequency separation $\Delta\nu$ where the decorrelation falls to 0.5 and 0.1 respectively i.e. $\kappa_U(\Delta\nu_{0.5}) = 0.5$, etc. Figure 7 shows $\Delta\nu_{0.5}$ and $\Delta\nu_{0.1}$ as functions of U. We use $\Delta\nu_{0.5}$ to compare and quantify how rapidly the signal decorrelates at different values of U. We see that $\Delta\nu_{0.5}$ has a nearly constant value ≈ 1 MHz for $U \leq 30$, and it declines as $U^{-0.6}$ for larger baselines in the range of our interest. The value of $\Delta\nu_{0.1}$ gives an estimate of the frequency separation across which the HI signal is correlated, and the bulk of the HI signal is contained within $\Delta\nu \leq \Delta\nu_{0.1}$. We see that $\Delta\nu_{0.1}$ has a nearly constant value ≈ 3 MHz at the small baselines ($U \leq 30$), and we have $\Delta\nu_{0.1} \approx 3 \times \Delta\nu_{0.5}$ for the entire baseline range of our interest.

Figures 6 and 7 provide an estimate of two of the system parameters, namely the total frequency bandwidth B and the frequency channel width $\Delta\nu_c$ desirable for quantifying the HI signal. We see that the HI signal remains correlated to frequency separations as large as 3 MHZ at the small baseline. It is thus desirable to have a bandwidth B larger than this, which is well within the specifications of both Phases I and II (Table 1). Considering the channel width, we see that $\Delta\nu_c = 10$ kHz or 20 kHz is small enough to adequately quantify the decorrelation of the HI signal at even the largest baseline of our interest. A larger channel width of $\Delta\nu_c = 200$ kHz will be

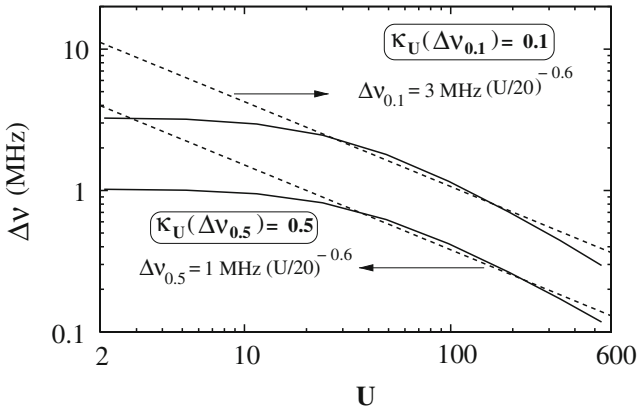

Figure 7. This figure shows how $\Delta\nu$ varies with functions of U for a given value of $\kappa_U(\Delta\nu)$. The upper and lower solid curves correspond to $\kappa_U(\Delta\nu_{0.1}) = 0.1$ and $\kappa_U(\Delta\nu_{0.5}) = 0.5$ respectively. The definition of $\Delta\nu_{0.1}$ and $\Delta\nu_{0.5}$ are given in the text. The dotted lines are power-law fitting for $\Delta\nu_{0.1}$ and $\Delta\nu_{0.5}$ to quantify how rapidly the signal decorrelates at different **U** values.

adequate for baselines $U \leq 200$, however some of the signal would be missed out at the large baselines ($U \sim 500$).

4.2 *Noise and error estimates*

We first consider the noise contribution $N_2(\mathbf{U}_n, \Delta\nu)$ to the visibility correlation (eq. (19)). The noise in the visibilities measured at different antenna pairs is uncorrelated. As noted earlier, the ORT has a high degree of redundancy and there are many independent antenna pairs corresponding to the same baseline. Further, an observation spanning a total observing time of $t_{\rm obs}$ provides $t_{\rm obs}/\Delta t$ different measurements of each visibility. The noise in the visibilities measured at two different time instants is uncorrelated. It is possible to avoid the noise contribution $N_2(\mathbf{U}_n, \Delta\nu)$ in the visibility correlation $V_2(\mathbf{U}_n, \Delta\nu)$ by correlating only the visibility measurements where the noise is uncorrelated (eg. Begum *et al*. 2006; Ali *et al*. 2008). For a fixed baseline $\mathbf{U}$ we only correlate the visibilities measured by different antenna pairs or the visibilities measured at different time instants. We therefore do not include the noise contribution to the visibility correlation in subsequent analysis, and use

$$V_2(\mathbf{U}_n, \Delta\nu) = S_2(\mathbf{U}_n, \Delta\nu) + F_2(\mathbf{U}_n, \Delta\nu)\,. \tag{26}$$

The noise however contributes to uncertainty in the visibility correlation $\sqrt{(\Delta V_2)^2}$ which we discuss below.

We now calculate the expected statistical fluctuations (errors) or uncertainty in the estimated visibility correlation $\mathcal{V}_2(U, \Delta\nu)$. It is assumed that the foregrounds have been completely removed from the visibilities whereby the residuals after foreground subtraction contain only the HI signal and system noise. Therefore the total error in the residual visibility correlation has two parts arising from the cosmic variance and the system noise respectively. The expected uncertainty or statistical fluctuations in the visibility correlation is

$$\sqrt{(\Delta V_2)^2} = \sqrt{(\Delta S_2)^2 + (\Delta N_2)^2}\,, \tag{27}$$

where $(\Delta S_2)^2$ and $(\Delta N_2)^2$ are the cosmic variance and the system noise contributions respectively.

We have $(\Delta N_2)^2 = (2\sigma^2)^2$ and $(\Delta S_2)^2 = (S_2)^2$ for a single estimate of the visibility correlation. The system noise contribution reduces to $(\Delta N_2)^2 = (2\sigma^2 \Delta t/t_{\rm obs})^2$ if we combine the measurements at different time instants. The redundant baselines provide many estimates of the visibility correlation $V_2(\mathbf{U}, \Delta\nu)$ at the same $\mathbf{U}$. Each estimate has an independent system noise contribution, but the signal however is the the same. We also bin the data by combining the estimates of $V_2(\mathbf{U}, \Delta\nu)$ at the different $\mathbf{U}$ values within a finite bin width of our choice. The different baselines $\mathbf{U}$ provide independent estimates of both the signal and the system noise. We use N_P and N_E respectively to denote the number of independent estimates of the system noise and the signal in $V_2(U, \Delta\nu)$ for each bin.

The frequency bandwidth B also provides several independent estimates of the visibility correlation. The value of $\Delta\nu_{0.5}$ provides an estimate of the frequency separation over which the HI signal remains correlated. For the purpose of the estimates presented here we assume a channel width of $\Delta\nu_{\rm c} = \Delta\nu_{0.5}$ in eq. (10) for σ^2 and also assume that the frequency bandwidth B provides us with $B/(\Delta\nu_{0.5})$

independent estimates of the visibility correlation. Combining all the effects discussed above we have

$$(\Delta N_2)^2 = \left(\frac{2\sigma^2\,\Delta t}{t_{\rm obs}}\right)^2 \frac{\Delta\nu_{0.5}}{N_P B} \tag{28}$$

and

$$(\Delta S_2)^2 = \frac{(S_2)^2 \Delta\nu_{0.5}}{N_E B} \tag{29}$$

which we use in eq. (27) to calculate the error estimates $\sqrt{(\Delta V_2)^2}$ for $S_2(U,0)$ and also the signal to noise ratio SNR$= S_2(U,0)/\sqrt{(\Delta V_2)^2}$. We have calculated N_P and N_E by dividing the baseline range $U_{\rm min}$ to $U_{\rm max}$ into 6 and 9 logarithmic bins for Phases I and II respectively.

The uncertainty $\sqrt{(\Delta V_2)^2}$ shown in Fig. 5 is dominated by the system noise over the entire baseline range. The SNR, shown in Fig. 8, peaks at $U \sim 100$ which corresponds to $\sim 30'$. This peak feature is particularly prominent for Phase II which also has a higher SNR compared to Phase I. We see that for Phase I, a 3σ detection is possible at $U \sim 100$ with ~4,000 h of observation. The SNR scales as $\propto t_{\rm obs}$, and a 5σ detection is possible with ~5,700 h of observation with Phase I.

The signal and noise in the individual visibilities are both larger for Phase II in comparison to Phase I (Table 1). The noise contribution to a single visibility scales as $\sigma \propto (bd)^{-1}$ (eq. (10)) whereas the signal scales as $\sqrt{V_2} \propto (bd)^{-0.5}$ (eq. (17)), and a single visibility has a lower SNR in Phase II as compared to Phase I. However, there is a substantial increase in the number of baselines for Phase II which more than compensates for this, and we find that the binned visibility correlation has a considerably higher SNR for Phase II in comparison to Phase I (Fig. 8). We see that a 3σ detection is possible with ~1,000 h of observation with Phase II. A 5σ detection is possible in the baseline range $40 \leq U \leq 100$ with ~2,000 h of observation. It is possible to detect the HI signal at a significance greater than 5σ in the baseline range $10 \leq U \leq 200$ with ~3,000 h of observation.

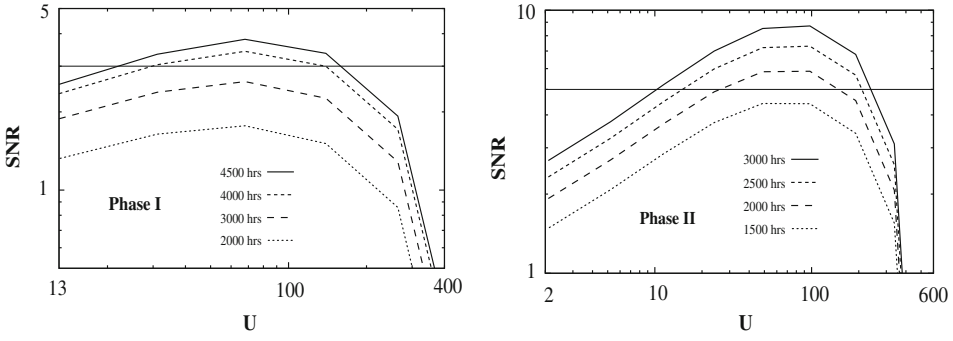

Figure 8. This figure shows the signal-to-noise ratio (SNR) as function of baseline **U** for different integration times as indicated. The horizontal line is for SNR = 5 (right panel) and SNR = 3 (left panel).

4.3 *Foregrounds*

We refer to radiation from different astrophysical sources other than the cosmological HI signal collectively as foregrounds. Foregrounds include extragalactic point sources, diffuse synchrotron radiation from our galaxy and low redshift galaxy clusters; free–free emission from our galaxy (GFF) and external galaxies (EGFF). Extra-galactic point sources and the diffuse synchrotron radiation from our galaxy largely dominate the foreground radiation at 326.5 MHz. The free–free emissions from our galaxy and external galaxies make much smaller contributions though each of these is individually larger than the HI signal. All the foreground components mentioned earlier are continuum sources. It is well accepted that the frequency dependence of the various continuum foreground components can be modelled by power laws, and we model the multi-frequency angular power spectrum for each foreground component as

$$C_\ell(\nu_1, \nu_2) = A \left(\frac{1000}{\ell}\right)^\gamma \left(\frac{\nu_f}{\nu_1}\right)^\alpha \left(\frac{\nu_f}{\nu_2}\right)^\alpha , \tag{30}$$

where A is the amplitude in mK^2, and γ and α are the power-law indices for the ℓ and the ν dependence respectively. In the present analysis, we are interested in a situation where $\nu_2 = \nu_1 + \Delta\nu$ with $\Delta\nu \ll \nu_1$, and we have

$$C_\ell(\Delta\nu) \equiv C_\ell(\nu_1, \nu_1 + \Delta\nu) \approx A \left(\frac{1000}{\ell}\right)^\gamma \left(\frac{\nu_f}{\nu_1}\right)^{2\alpha} \left(1 - \frac{\alpha\,\Delta\nu}{\nu_1}\right) \tag{31}$$

which varies slowly with $\Delta\nu$. For the foregrounds, we expect $C_\ell(\Delta\nu)$ to fall by less than 10% if $\Delta\nu$ is varied from 0 to 3 MHz, in contrast to the $\sim$90% decline predicted for the HI signal (Fig. 7). The frequency spectral index α is expected to have a scatter $\Delta\alpha$ in the range 0.1−0.5 for the different foreground components in different directions causing less than 2% additional deviation in the frequency band of our interest. We only consider the mean spectral indices for the purpose of the foreground predictions presented here. In a nutshell, the $\Delta\nu$ dependence of $C_\ell(\Delta\nu)$ is markedly different for the foregrounds as compared to the HI signal and we hope to use this to separate the foregrounds from the HI signal.

There are, at present, no observational constraints on the $\Delta\nu$ dependence of $C_\ell(\Delta\nu)$ for any of the foreground components at the angular scales and frequencies of our interest. We do not attempt to make any model predictions for the $\Delta\nu$ dependence beyond assuming that $C_\ell(\Delta\nu)$ varies slowly with $\Delta\nu$ across the frequency separations of our interest. For the present work, we focus on $C_\ell(0)$ which we have modelled as

$$C_\ell(0) = A \left(\frac{1000}{\ell}\right)^\gamma , \tag{32}$$

and we assume that the $\Delta\nu$ dependence is very slow whereby the foregrounds can be separated from the HI signal. In the subsequent discussion we focus on model predictions for A and γ which are tabulated in Table 3 for the different foreground components. The values of A, whenever used in this paper, have all been scaled ($A \propto \nu^{-2\alpha}$) to the nominal frequency of $\nu_o = 326.5$ MHz using the α values tabulated in Table 3.

Table 3. Values of the parameters used for characterizing different foreground contributions at 326.5 MHz.

Foregrounds	A (mk^2)	α	γ
Point source (Poisson)	$288\left(\frac{S_c}{\mathrm{Jy}}\right)^{1.36}+0.01$	2.7	0
Point source (clustered)	$453\left(\frac{S_c}{\mathrm{Jy}}\right)^{0.72}-112\left(\frac{S_c}{\mathrm{Jy}}\right)^{0.36}+161$	2.7	0.9
Galactic synchrotron	10.2	2.52	2.34
Galactic free–free	1.7×10^{-3}	2.15	3.0
Extragalactic free–free	2.3×10^{-4}	2.1	1.0
HI signal	1.1×10^{-6}	–	–

Extragalactic point sources are expected to dominate the 326.5 MHz sky at the angular scales of our interest. The contribution from extragalactic point sources is mostly due to the emission from normal galaxies, radio galaxies, star forming galaxies and active galactic nuclei (Santos *et al*. 2005). Predictions of the point source contribution are based on the measured source count function and the angular correlation function.

There are different radio surveys that have been conducted at various frequencies ranging from 151 MHz to 8.5 GHz, and these have a wide range of angular resolutions ranging from $1''$ to $5'$ (e.g. Singal *et al*. 2010, and references therein). There is a clear consistency among the differential source count functions $\left(\frac{\mathrm{d}N}{\mathrm{d}S}\propto S^{-\epsilon}\right)$ at 1.4 GHz for sources with flux $S > 1$ mJy. The source counts are poorly constrained at $S < 1$ mJy. Based on the various radio observations (Singal *et al*. 2010), we have identified four different regimes for the 1.4 GHz source counts: (a) $\gtrsim$1 Jy which are the brightest sources in the catalogs. These are relatively nearby objects and they have a steep, Euclidean source count with $\epsilon \sim 2.5$; (b) 1 mJy–1 Jy where the observed differential source counts decline more gradually with $\epsilon \sim 1.7$ which is caused by redshift effects; (c) 15 μJy–1 mJy where the source counts are again steeper with $\epsilon > 2$ which is closer to Euclidean, and there is considerable scatter from field to field; and (d) $\lesssim$ 15 μJy, the source counts must eventually flatten ($\epsilon < 2$) at low S to avoid an infinite integrated flux. The cut-off lower flux where the power law index ϵ falls below 2 is not well established, and deeper radio observations are required.

If we extrapolate the 1.4 GHz source counts to 326.5 MHz, the power law index ϵ remains unchanged, but the flux range and the constant of proportionality change. This change depends upon the value of the frequency spectral index used to extrapolate from 1.4 GHz to 326.5 MHz.

The first turnover or flattening in the 1.4 GHz differential source count has been reported at $\sim$ 1 mJy (Condon 1989; Rowan-Robinson *et al*. 1993; Hopkins *et al*. 1998; Richards 2000; Hopkins *et al*. 2003; Seymour *et al*. 2004; Jarvis & Rawlings 2004; Huynh *et al*. 2005; Simpson *et al*. 2006; Owen & Morrison 2008). The flatenning is attributed to the emergence of a new population of radio sources (star-forming galaxies and low-luminosity AGN) below $\sim$ 1 mJy. The turnover flux of 1 mJy at 1.4 GHz is equivalent to $\sim$3 mJy at 325 MHz assuming a spectral index of 0.7. This is

consistent with 325 MHz GMRT observations (Sirothia *et al*. 2009). These features have also been observed at $S \sim 1.9$ mJy in 610 MHz GMRT observations (Garn *et al*. 2007; Bondi *et al*. 2007; Garn *et al*. 2008).

We have modelled the 326.5 MHz source count function using a double power law

$$\frac{\mathrm{d}N}{\mathrm{d}S} = \begin{cases} \frac{4000}{\mathrm{Jy\cdot Sr}} \cdot \left(\frac{S}{1\,\mathrm{Jy}}\right)^{-1.64} & \text{for } 3\,\mathrm{mJy} \leq S \leq 3\,\mathrm{Jy}, \\ \frac{134}{\mathrm{Jy\cdot Sr}} \cdot \left(\frac{S}{1\,\mathrm{Jy}}\right)^{-2.24} & \text{for } 10\,\mu\mathrm{Jy} \leq S \leq 3\,\mathrm{mJy}\,. \end{cases} \tag{33}$$

Here we have fitted the 325 MHz differential source count measured by Sirothia *et al*. (2009) to obtain the power law for $S \geq 3$ mJy. This measurement, which is the deepest till date at this frequency, does not adequately cover sources fainter than 3 mJy. For sources below 3 mJy, we fit 1.4 GHz source counts from extremely deep VLA observations (Hubble Deep Field-North; Biggs & Ivison 2006) in the flux range 30 μJy to 1153 μJy by a single power law with slope $\epsilon = 2.24$. We scale this to 326.5 MHz using an average spectral index of 0.7 (Jackson 2005; Randall *et al*. 2012). As mentioned earlier, the lower cut-off below which the source count flattens is not well determined. For the purpose of this paper, we assume that the power law behaviour $S^{-2.24}$ holds for $S \geq 10\,\mu$Jy, and the source count is flatter than S^{-2} (we use $\epsilon = 1.5$, Condon *et al*. 2012) for sources fainter than this. The choice of 10 μJy is motivated by the fact that the total contribution from sources with flux $S \leq 10\,\mu$Jy to each pixel in the sky converges to $\sim 10\,\mu$Jy for a pixel size of $\sim 2'$ which is comparable to the N–S resolution of the ORT.

Point sources make two distinct contributions to the angular power spectrum, the first being the Poisson fluctuation due to the discrete nature of the sources and the second arising from the clustering of the sources. The Poisson contribution, which is independent of ℓ, is calculated using

$$C_\ell(0) = \left(\frac{\partial B}{\partial T}\right)^{-2} \left[\int_0^{S_c} S^2 \frac{\mathrm{d}N}{\mathrm{d}S}\,\mathrm{d}S\right], \tag{34}$$

where S_c (≤ 3 Jy) is the cut-off flux, all point sources brighter than this are assumed to have been identified and subtracted out from the data. The Poisson contribution is dominated by the brightest sources ($S \sim S_\mathrm{c}$), and the 10 μJy lower cut-off does not make a significant contribution to the amplitude A listed in Table 3.

The analysis of large samples of nearby radio-galaxies has shown that the point sources are clustered. Cress *et al*. (1996) have measured the angular two point correlation function at 1.4 GHz (FIRST Radio Survey, Becker *et al*. 1995) across angular scales of $1.2'$ to $2°$, equivalent to a $\mathbf{U}$ range of $14 < \mathbf{U} < 1430$. The measured two-point correlation function can be well fitted with a single power law

$$w(\theta) = (\theta/\theta_0)^{-\beta}, \tag{35}$$

where $\beta = 1.1$ and $\theta_0 = 17.4'$. They have also reported that the double and multi-component sources tend to have a larger clustering amplitude than the whole sample on small scales ($\leq 12'$). Further, the sources with flux below 2 mJy have a shallower slope ($\beta \sim 0.97$).

For the purpose of this paper we have modeled the angular power spectrum due to the clustering of point sources as

$$C_\ell(0) = \left(\frac{\partial B}{\partial T}\right)^{-2} \left[\int_0^{S_c} S \frac{\mathrm{d}N}{\mathrm{d}S}\,\mathrm{d}S\right] w_\ell \ , \tag{36}$$

where $w_\ell \propto \ell^{\beta-2}$ is the Legendre transform of $w(\theta)$. In this case, the amplitude A listed in Table 3 is sensitive to both the upper cut-off S_c and the lower cut-off of 10 μJy. However, in reality the faint sources have a weaker clustering as compared to the single power law adopted here, and we do not expect a very significant dependence on the lower cut-off of 10 μJy.

The galactic diffuse synchrotron radiation is believed to be produced by cosmic ray electrons propagating in the magnetic field of the galaxy (Ginzburg & Syrovatskii 1969; Rybicki & Lightman 1979). La Porta *et al.* (2008) have determined the angular power spectra of the galactic synchrotron emission at angular scales greater than 0.5° using total intensity all-sky maps at 408 MHz (Haslam *et al.* 1982) and 1.42 GHz (Reich 1982; Reich & Reich 1986; Reich *et al.* 2001). They found that the angular power spectrum of synchrotron emission is well described by a power law (eq. (32)) where the value of γ varies in the range 2.6 to 3.0 depending on the galactic latitude. Further, they have analysed the frequency dependence to find $A \propto \nu^{-2\alpha}$ with α varying in the range 2.9 to 3.2.

The angular power spectrum of the galactic synchrotron radiation has been recently measured at angular scales less than 0.5° in three different 150 MHz observations. Bernardi *et al.* (2009) have estimated $\gamma = 2.2$ and $A = 253\,\mathrm{mK}^2$ using WSRT observations in a field with galactic latitude $b = 8°$. Ghosh *et al.* (2012) have estimated $\gamma = 2.34$ and $A = 513\,\mathrm{mK}^2$ using GMRT observations in a field with galactic latitude $b = 14°$. Iacobelli *et al.* (2013) have estimated $\gamma = 1.84$ using LOFAR observations in the same field as Bernardi *et al.* (2009). The mean spectral index of the synchrotron emission at high galactic latitude has been recently constrained to be $\alpha = 2.52$ in the 150−408 MHz frequency range (Rogers & Bowman 2008) using single dish observations. For the purpose of this paper we have used A and γ from Ghosh *et al.* (2012) and extrapolated this to 326.5 MHz using α from Rogers & Bowman (2008). The parameters for the galactic and extra-galactic free–free emission have been extrapolated from 130 MHz (Santos *et al.* 2005), and are listed in Table 3. For comparison, the value of $C_\ell(0)$ at $\ell = 1{,}000$ for the HI signal is also shown in Table 3.

Figure 9 shows the total expected sky signal assuming that the brightest source in the field has a flux of $S_c = 1$ Jy. The predictions are shown for Phase II, and $F_2(\mathbf{U}, 0)$ can be scaled by a factor of 6 to obtain the predictions for Phase I. The baseline range $U \leq 10$ is dominated by the synchrotron radiation, whereas $10 \leq U \leq 300$ is dominated by the clustering of the point sources and $U \geq 300$ is dominated by the Poisson contribution. The contributions from the galactic and extra-galactic free–free emission are considerably smaller across the entire U range. We find that the total foreground contribution to each visibility is around 10^4–10^5 times larger than the HI signal.

It is very important to correctly identify the point sources and subtract these out at a high level of precision (∼10−100 mJy) in order to detect the HI signal (Ali *et al.* 2008; Bowman *et al.* 2009; Bernardi *et al.* 2011; Pindor *et al.* 2011; Ghosh *et al.*

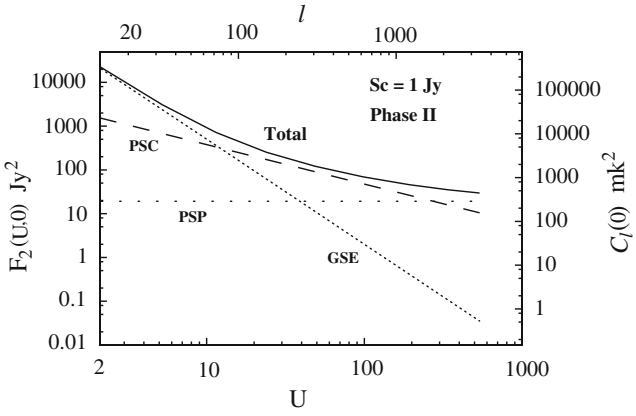

Figure 9. This shows the foreground model predictions for Phase II under the assumption that the brightest source in the field has a flux of $S_c = 1$ Jy. The left and bottom axes respectively show $F_2(\mathbf{U}, 0)$ as a function of $\mathbf{U}$, while the right and top axes respectively show $C_\ell(0)$ as a function of ℓ. In addition to the total foregrounds, the individual components are namely Point Source Clustering (PSC), Point Source Poisson (PSP) and Galactic Synchrotron Emission (GSE). The Galactic Free–Free (GFF) and the Extra-Galactic Free–Free (EGFF) components which are relatively much weaker, have not been shown but they have in total foreground predictions.

2012). Here we assume that sources with flux density $S \geq S_c$ are visually identified and perfectly subtracted out from the data. The left and right panels of Fig. 10 shows the foreground predictions for $S_c = 100$ mJy and 10 mJy respectively. The galactic synchrotron radiation is the most dominant component at $\mathbf{U} \leq 50$ (i.e. $\theta \geq 34'$) and ≤ 100 (i.e. $\theta \geq 17'$) for $S_c = 100$ mJy and 10 mJy respectively. The point source clustering component dominates at larger baselines or small angular scales. The Poisson contribution falls faster than the clustering contribution as S_c is reduced, and it is sub-dominant at all U.

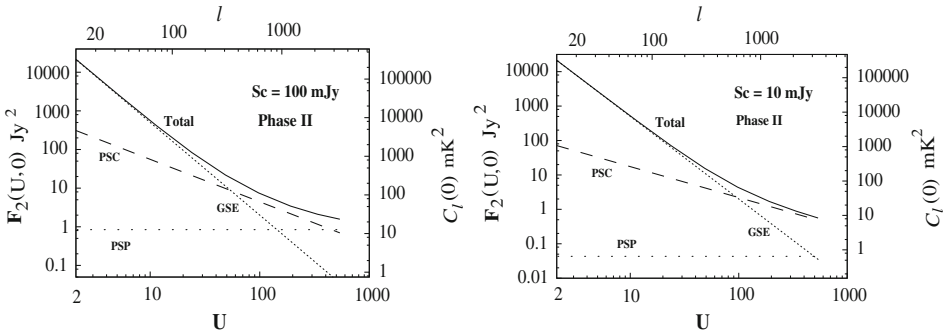

Figure 10. Same as Fig. 9 except that we assume that the point sources-brighter than $S_c = 100$ mJy (left panel), and $S_c = 10$ mJy (right panel) have been identified and subtracted out from the data. The GFF and EGFF components, which are relatively much weaker, have not been shown.

The confusion limit is predicted to be ∼175 mJy for ORT (Phase II). However, we do not propose to identify and subtract point sources using one dimensional ORT images. We plan to use existing 325 MHz source catalogues (e.g. the Westerbork Northern Sky Survey (WENSS); Rengelink 1997) or GMRT observations to identify point sources in the ORT field-of-view and subtract their contribution for the ORT visibility data. The WENSS survey has a thresold flux density of 18 mJy, whereas the deepest GMRT observation (Sirothia *et al*. 2009) has achieved a thresold flux density of 0.27 mJy at this frequency.

The residual foregrounds, after point source subtractions, are still $\sim 10^4$ times the HI signal. As mentioned earlier, we expect $F_2(U, \Delta\nu)$ to have a smooth $\Delta\nu$ dependence and remain correlated across $\Delta\nu \sim 5$ MHZ whereas the HI signal is expected to decorrelate within this frequency interval. It is thus, in principle, possible to use the distinctly different $\Delta\nu$ dependence to separate the HI signal from the foregrounds. This foreground removal technique has been demonstrated to work in 610 MHz GMRT observations where it was possible to completely remove the foregrounds so that the residuals were consistent with the cosmological HI signal and noise (Ghosh *et al*. 2011b). We propose to use a similar technique for foreground removal from the ORT data.

5. Summary and conclusions

The ORT is currently being upgraded to operate as a radio-interferometer. The upgrade is being carried out in two different stages with two nearly independent systems, namely Phase I and Phase II, being expected at the end of the upgrade. We have briefly discussed these two phases and the relevant parameters are presented in Table 1. The telescope has a nominal frequency of 326.5 MHz which corresponds to the HI signal from the redshift $z = 3.35$.

Phases I and II respectively cover the angular multipole range $80 \leq \ell \leq 3100$ and $10 \leq \ell \leq 3500$, which correspond to the Fourier modes in the range $1.2 \times 10^{-2} \leq \mathbf{k}_\perp \leq 5.0 \times 10^{-1}\,\mathrm{Mpc}^{-1}$ and $2.0 \times 10^{-3} \leq \mathbf{k}_\perp \leq 5.4 \times 10^{-1}\,\mathrm{Mpc}^{-1}$ for the 3D HI power spectrum (Fig. 3). We see that Phases I and II are both sensitive to the BAO feature which has the first peak at $k = 4.5 \times 10^{-2}\,\mathrm{Mpc}^{-1}$. The successive oscillations also are well within the k range that will be probed.

We have made detailed predictions for both, the HI signal and the foregrounds expected in Phases I and II. The foregrounds, we found, are dominated by the galactic synchrotron emission at large angular scales whereas the contribution from the clustering of point sources dominates at small angular scales. It is very important to correctly identify the point sources and subtract them from the data. We find that the galactic synchrotron emission dominates at $\ell \leq 630$ and the contribution from the clustering of point sources dominates at $\ell > 630$ if we assume that it is possible to identify and subtract all the point sources brighter than $S_c = 10$ mJy (Fig. 10). The foreground contribution to the individual visibilities is predicted to be around $10^4 - 10^5$ times larger than the HI signal (Fig. 5). Foreground removal is a big challenge for detecting the HI signal.

The HI signal at a fixed angular multipole ℓ but at two different frequencies ν and $\nu + \Delta\nu$, we found, decorrelates rapidly as $\Delta\nu$ is increased (Fig. 6). The HI signal is found to be totally decorrelated for $\Delta\nu \geq 3$ MHz for the entire ℓ range of our

interest (Fig. 7). In contrast, the foregrounds originate from continuum sources, and we expect the foregrounds to remain correlated across $\Delta\nu \sim 3$ MHz. We propose to use this property to extract the HI signal from the foregrounds.

We have investigated the SNR for detecting the HI signal under the assumption that it is possible to completely remove the foregrounds. For both Phases I and II, the SNR peaks around the baseline $U \sim 100$ which corresponds to the angular multipole $\ell \sim 630$ (Fig. 8). We see that for Phase I, a 3σ detection is possible with ∼4,000 h of observation and a 5σ detection is possible with ∼5,700 h of observation. A 3σ detection is possible with ∼1,000 h of observation with Phase II, and a detection better than $> 5\sigma$ is possible with ∼2,000 h of observation.

The present paper primarily introduces the ORT as an instrument for exploring the high redshift cosmological HI signal, and presents the expected signal and foreground contributions. Preliminary SNR estimates have been presented, and these have been used to estimate the observing time required to detect the HI signal. We plan to perform a more rigorous analysis of power spectrum and parameter estimation in subsequent work, and also address the possibility of detecting the BAO feature.

Acknowledgements

The authors would like to thank Jayaram N. Chengalur and C. R. Subrahmanya for involving and motivating them in this project. The authors would also like to thank P. K. Manoharan and Visweshwar Ram Marthi for their help with many technical details of the ORT system. The authors also thank Abhik Ghosh, Jasjeet S. Bagla, Peeyush Prasad and Shiv K. Sethi for useful discussions. SSA would like to acknowledge CTS, IIT Kharagpur for the use of its facilities and the support by DST, India, under Project No. SR/FTP/PS-088/2010. SSA would also like to thank the authorities of IUCAA, Pune, India for providing the Visiting Associateship programme.

References

Ali, S. S., Bharadwaj, S., Pandey, B. 2005, *MNRAS*, **363**, 251.
Ali, S. S., Bharadwaj, S., Chengalur, J. N. 2008, *MNRAS*, **385**, 2166.
Bagla, J. S., Nath, B., Padmanabhan, T. 1997, *MNRAS*, **289**, 671.
Bagla, J. S., Khandai, N., Datta, K. K. 2010, *MNRAS*, 931.
Barkana, R., Loeb, A. 2005, *ApJl*, **624**, L65.
Barkana, R. 2006, *MNRAS*, **372**, 259.
Becker, R. H., White, R. L., Helfand, D. J. 1995, *ApJ*, **450**, 559.
Begum, A., Chengalur, J. N., Bhardwaj, S. 2006, *MNRAS*, **372**, L33.
Bernardi, G. *et al.* 2009, *A&A*, **500**, 965.
Bernardi, G., Mitchell, D. A., Ord, S. M. *et al.* 2011, *MNRAS*, **413**, 411.
Bharadwaj, S., Nath, B., Sethi, S. K. 2001, *JApA*, **22**, 21.
Bharadwaj, S., Sethi, S. K. 2001, *JApA*, **22**, 293.
Bharadwaj, S., Ali, S. S. 2004, *MNRAS*, **352**, 142.
Bharadwaj, S., Ali, S. S. 2005, *MNRAS*, **356**, 1519.
Bharadwaj, S., Sethi, S., Saini, T. D. 2009, *Phys Rev. D*, **79**, 083538.
Bharadwaj, S., Pandey, S. K. 2003, *JApA*, **24**, 23.
Biggs, A. D., Ivison, R. J. 2006, *MNRAS*, **371**, 963.
Bondi, M., Ciliegi, P., Venturi, T. *et al.* 2007, *AAP*, **463**, 519.

Bowman, J. D. *et al.* 2009, *ApJ*, **695**, 183.
Busca, N. G., Delubac, T., Rich, J. *et al.* 2013, *AAP*, **552**, A96.
Chang, T.-C., Pen, U.-L., Peterson, J. B., McDonald, P. 2008, *Phys Rev. Lett.*, **100**, 091303.
Cho, J., Lazarian, A., Timbie, P. T. 2012, *Ap.J*, **749**, 164.
Condon, J. J. 1989, *ApJ*, **338**, 13.
Condon, J. J., Cotton, W. D., Fomalont, E. B. *et al.* 2012, *ApJ*, **758**, 23.
Cress, C. M., Helfand, D. J., Becker, R. H., Gregg, M. D., White, R. L. 1996, *ApJ*, **473**, 7.
Di Matteo, T., Perna, R., Abel, T., Rees, M.J. 2002, *ApJ*, **564**, 576.
Datta, K. K., Roy Choudhury, T., Bharadwaj, S. 2007, *MNRAS*, **378**, 119.
Datta, A., Bowman, J. D., Carilli, C. L. 2010, *ApJ*, **724**, 526.
Dillon, J. S., Liu, A., Williams, C. L. *et al.* 2013, arXiv:1304.4229.
Eisenstein, D. *et al.* 2005, *ApJ*, **633**, 560.
Furlanetto, S. R., Oh, S. P., Briggs, F. H. 2006, *Phys. Rep.*, **433**, 181.
Garn, T., Green, D. A., Hales, S. E. G., Riley, J. M., Alexander, P. 2007, *MNRAS*, **376**, 1251.
Garn, T., Green, D. A., Riley, J. M., Alexander, P. 2008, *MNRAS*, **383**, 75.
Ghosh, A., Bharadwaj, S., Ali, S. S., Chengalur, J. N. 2011a, *MNRAS*, **411**, 2426.
Ghosh, A., Bharadwaj, S., Ali, S. S., Chengalur, J. N. 2011b, *MNRAS*, **418**, 2584.
Ghosh, A., Prasad, J., Bharadwaj, S., Ali, S. S., Chengalur, J. N. 2012, *MNRAS*, **426**, 3295.
Ginzburg, V. L., Syrovatskii, S. I. 1969, *Ann. Rev. Astron. Astrophys.*, **7**, 375.
Guha Sarkar, T., Mitra, S., Majumdar, S., Choudhury, T. R. 2012, *MNRAS*, **421**, 3570.
Harker, G. *et al.* 2009, *MNRAS*, **397**, 1138.
Haslam, C. G. T., Stoffel, H., Salter, C. J., Wilson, W. E. 1982, *A&AS*, **47**, 1.
Hopkins, A. M., Mobasher, B., Cram, L., Rowan-Robinson, M. 1998, *MNRAS*, **296**, 839.
Hopkins, A. M., Afonso, J., Chan, B. *et al.* 2003, *A.J*, **125**, 465.
Huynh, M. T., Jackson, C. A., Norris, R. P., Prandoni, I. 2005, *AJ*, **130**, 1373.
Iacobelli, M., Haverkorn, M., Orrú, E. *et al.* 2013, arXiv:2804.1308.
Jacobs, D. C., Bowman, J., Aguirre, J. E. 2013, *ApJ*, **769**, 5.
Jelic, V., Zaroubi, S., Labropoulos, P., Bernardi, G, de Bruyn, A. G., Koopmans, L. V. E. 2010, *MNRAS*, **409**, 1647.
Jarvis, M. J., Rawlings, S. 2004, *New Astron. Rev.*, **48**, 1173.
Jackson, C. 2005, *PASA*, **22**, 36.
Kumar, A., Padmanabhan, T., Subramanian, K. 1995, *MNRAS*, **272**, 544.
La Porta, L., Burigana, C., Reich, W. *et al*. 2008, *A&A*, **479**, 641.
Loeb, A., Wyithe, J. S. B. 2008, *Phys. Rev. Lett.*, **100**, 161301.
Loeb, A., Zaldarriaga, M. 2004, *Phys. Rev. Lett.*, **92**, 211301.
Liu, A., Tegmark, M. 2011, *PhReD*, **83**, 103006.
Liu, A., Tegmark, M. 2012, *MNRAS*, **419**, 3491.
Madau, P., Meiksin, A., Rees, M. J. 1997, *ApJ*, **475**, 429.
Majumdar, S., Bharadwaj, S., Choudhury, T. R. 2013, *MNRAS*, **434**, 1978.
Mao, X.-C. 2012, *Ap.J*, **744**, 29.
Mao, Y. *et al.* 2012, *MNRAS*, **422**, 926.
Marín, F. A., Gnedin, N. Y., Seo, H.-J., Vallinotto, A. 2010, *Ap.J*, **718**, 972.
Masui, K. W., McDonald, P., Pen, U.-L. 2010, *PhReD*, **81**, 103527.
Masui, K. W., Switzer, E. R., Banavar, N. *et al.* 2013, *Ap.JL*, **763**, L20.
Mauch, T., Murphy, T., Buttery, H. J. *et al.* 2003, *MNRAS*, **342**, 1117.
Moore, D. F., Aguirre, J. E., Parsons, A. R., Jacobs, D. C., Pober, J. C. 2013, *ApJ*, **769**, 154.
Noterdaeme, P., Petitjean, P., Carithers, W. C. *et al.* 2012, *AAP*, **547**, L1.
Nusser, A. 2005, *MNRAS*, **364**, 743.
Oh, S. Peng., Mack, K. J. 2003, *MNRAS*, **346**, 871.
Owen, F. N., Morrison, G. E. 2008, *AJ*, **136**, 1889.
Pen, U.-L., Staveley-Smith, L., Peterson, J. B., Chang, T.-C. 2009, *MNRAS*, **394**, L6.
Parsons, A. R. *et al.* 2010, *AJ*, **139**, 1468.

Pindor, B., Wyithe, J. S. B., Mitchell, D. A., Ord, S. M., Wayth, R. B., Greenhill, L. J. 2011, *Publ. Astron. Soc. Aust.*, **28**, 46.
Pober, J. C., Parsons, A. R., Aguirre, J. E. *et al.* 2013, *ApJl*, **768**, L36.
Prasad, P., Subrahmanya, C. R. 2011a, arXiv:1102.0148.
Prasad, P., Subrahmanya, C. R. 2011b, *Experimental Astron.*, **31**, 1.
Randall, K. E., Hopkins, A. M., Norris, R. P. *et al.* 2012, *MNRAS*, **421**, 1644.
Ram Marthi, V., Chengalur, J. 2013, arXiv:1310.1449.
Rowan-Robinson, M., Benn, C. R., Lawrence, A., McMahon, R. G., Broadhurst, T. J. 1993, *MNRAS*, **263**, 123.
Reich, W. 1982, *AAPS*, **48**, 219.
Reich, P., Reich, W. 1986, *A&AS*, **63**, 205.
Reich, P., Testori, J. C., Reich, W. 2001, *A&A*, **376**, 861.
Rengelink, R. B. *et al.* 1997, *Astron. Astrophys. Suppl. Ser.*, **124**, 259.
Richards, E. A. 2000, *ApJ*, **533**, 611.
Rogers, A. E. E., Bowman, J. D. 2008, *ApJ*, **136**, 641.
Rybicki, G. B., Lightman, A. P. 1979, Radiative Processes in Astrophysics, John Wiley & Sons, Hoboken, pp. 167.
Seo, H.-J., Dodelson, S., Marriner, J., Mcginnis, D., Stebbins, A., Stoughton, C., Vallinotto, A. 2010, *ApJ*, **721**, 164.
Singal, J., Stawarz, Ł., Lawrence, A., Petrosian, V. 2010, *MNRAS*, **409**, 1172.
Sirothia, S. K., Dennefeld, M., Saikia, D. J., Dole, H., Ricquebourg, F., Roland, J. 2009, *MNRAS*, **395**, 269.
Santos, M. G., Cooray, A., Knox, L. 2005, *ApJ*, **625**, 575.
Sarma, N. V. G., Joshi, M. N., Bagri, D. S., Ananthakrishnan, S. 1975, *J. Instn Electronics Telecommun. Engr.*, **21**, 110.
Seymour, N., McHardy, I. M., Gunn, K. F. 2004, *MNRAS*, **352**, 131.
Shaw, J. R., Sigurdson, K., Pen, U.-L., Stebbins, A., Sitwell, M. 2013, arXiv:1302.0327.
Simpson, C. *et al.* 2006, *MNRAS*, **372**, 741.
Subrahmanya, C. R., private communication.
Switzer, E. R., Masui, K. W., Bandura, K. *et al.* 2013a, *MNRAS*, **434**, L46.
Switzer, E. R., Masui, K. W., Bandura, K. *et al.* 2013b, arXiv:1304.3712.
Swarup, G., Sarma, N. V. G., Joshi, M. N., Kapahi, V. K., Bagri, D. S., Damle, S. H., Ananthakrishnan, S., Balasubramanian, V., Bhave, S. S., Sinha, R. P. 1971, *Nature Phys. Sci.*, **230**, 185.
Swarup, G., Ananthakrishnan, S., Kapahi, V. K., Rao, A. P., Subrahmanya C. R., Kulkarni, V. K. 1991, *Curr. Sci.*, **60**, 95.
Thompson, A. R., Moran, J. M., Swenson, G. W. 1986, Interferometry and Synthesis in Radio Astronomy, John Wiley & Sons, pp. 160.
Visbal, E., Loeb, A., Wyithe, S. 2009, *JCAP*, **10**, 30.
Wang, X., Hu, W. 2006, *ApJ*, **643**, 585.
Wyithe, S., Loeb, A. 2008, arXiv:2323.0808.
Wyithe, S., Loeb, A., Geil, P. 2007, arXiv:2955.0709.
Zafar, T., Péroux, C., Popping, A. *et al.* 2013, *AAP*, **556**, A141.